Ferrite Beads Design to Improve Turn-off Characteristics of Cascode GaN HEMTs: An Optimum Design Method.

Xue, Peng; Iannuzzo, Francesco

Published in:
IEEE Journal of Emerging and Selected Topics in Power Electronics

DOI (link to publication from Publisher):
10.1109/JESTPE.2023.3265903

Publication date:
2023

Document Version
Early version, also known as pre-print

Ferrite Beads Design to Improve Turn-off Characteristics of Cascode GaN HEMTs: An Optimum Design Method.

Peng Xue, *Member, IEEE* and Francesco Iannuzzo, *Senior Member, IEEE*

***Abstract*—In this paper, an optimum ferrite beads design method is proposed to suppress the self-sustained turn-off oscillation of cascode gallium nitride high-electron-mobility transistors (GaN HEMTs). At first, the impacts of gate loop beads and power loop beads on the turn-off oscillation of cascode GaN HEMTs are analyzed. The analysis reveals the weak damping effect of gate loop beads on the turn-off oscillation. Next, an analytical method is proposed to design the power loop beads that can achieve maximum effective damping on the turn-off oscillation. The power loop beads introduce extra stray inductance in the power loop, which can induce high voltage overshoot. To tackle the problem, an optimum design method is proposed so that the power loop beads can suppress the oscillation while mitigating the voltage overshoot. The accuracy of the proposed model is validated by the experimental data in the end.**

***Index Terms*—gallium nitride (GaN), GaN cascode HEMTs, ferrite beads, turn-off oscillation, self-sustained oscillation**

I. Introduction

The high turn-off speed of cascode gallium nitride high-electron-mobility transistors (GaN HEMTs) make them a suitable candidate for high-frequency power conversion applications with high turn-off current [1], [2]. Despite the merit, the cascode GaN HEMTs have a well-known problem of underdamped current and voltage oscillation during the turn-off transient [3]–[7]. Due to the cascode configuration, the stray elements in the gate loop of depletion-mode HEMT (DHEMT) form an LC tank which lacks effective damping [6]. This makes the cascode GaN HEMTs based half-bridge circuit very unstable and prone to generate underdamped turn-off oscillation. In the worst-case scenario, the underdamped turn-off oscillation can become self-sustained [4], [8]. The self-sustained oscillation can induce very severe electromagnetic Interference (EMI) problems, which need to be avoided in power conversion applications.

To tackle this problem, many suppression methods have been proposed in previous research. As one of the most readily applicable solutions, the utilization of ferrite beads is discussed in many previous studies to suppress the turn-off oscillation. In [9], SPICE simulation is performed with a ferrite bead utilized in the gate of cascode GaN HEMT. The simulation shows that the gate loop beads can slightly dampen the gate voltage ringing. In the application note provided by the Transphorm [10], [11], the ferrite beads are recommended to be utilized in the gate loop and power loop to suppress the switching oscillation of cascode GaN HEMT. In [12], the double-pulse test is performed with a ferrite bead utilized in the gate loop and very severe oscillation are observed in the turn-off waveforms. In [13], the ferrite beads are utilized either in the gate loop or power loop to suppress the switching oscillation of cascode GaN HEMT. It is identified that the gate loop bead has a relatively weak damping effect on the switching oscillation. On the other hand, the power loop bead has a very strong damping effect and can greatly suppress the oscillation. In [14], the test is performed on a GaN cascode HEMT based boost converter with and without ferrite beads in power loop. The test results show the power loop beads can greatly dampen the switching oscillation of cascode GaN HEMT.

The studies presented in [9]–[13] provide diverse opinions on the utilization of gate loop beads in cascode GaN HEMTs based circuits. Although the gate loop beads are recommended in [10], [11], the other papers [9], [12], [13] show the gate loop beads have a relatively weak damping effect on the oscillation. The impact of the gate loop beads on the turn-off oscillation has to be further investigated. Many research [10], [13], [14] show that the power loop beads have a great damping effect on the turn-off oscillation of cascode GaN HEMTs. However, the beads also introduce additional stray inductance in the power loop. If improper power loop beads are utilized, the stray inductance can induce extra oscillation [15], [16]. Therefore, it is necessary to find the optimum design of the power loop beads which can suppress the oscillation without introducing extra oscillation.

Looking into the previous research, only a few papers are published on the application of ferrite beads in cascode GaN HEMTs based circuit [9]–[14]. In [10], [11], the manufacturer recommend some typical ferrite beads applications in the cascode GaN HEMTs based half-bridge circuit. The studies [9], [12] show the impact of the gate loop beads on the switching oscillation. In [13], the effective damping of gate loop and power loop beads on the switching oscillation are experimentally investigated. The utilization of power loop beads to suppress the switching oscillation of cascode GaN HEMT is briefly discussed in [14]. Unfortunately, none of the the studies mentioned the ferrite beads design method. Since the self-sustained turn-off oscillation of cascode GaN HEMTs causes severe electromagnetic Interference (EMI) problems and can disrupt the converter operation, a ferrite beads design method is highly demanded to suppress the oscillation.

The goal of this paper is to propose an optimum ferrite beads design method to suppress the self-sustained oscillation of

The authors are with the Energy Technology Department, Aalborg University, Aalborg East 9220, Denmark. (E-mail: pexu@energy.aau.dk).

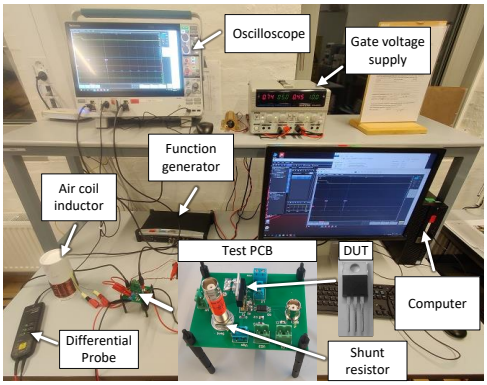

(a) The test platform.

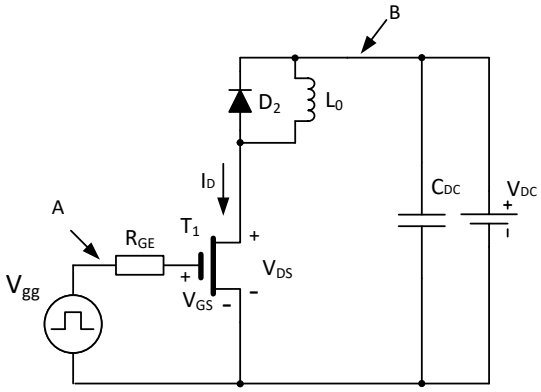

(b) The schematic circuit.

Fig. 1. Double-pulse test setup. (a) Test platform. (b) Schematic of double-pulse test circuit.

cascode GaN HEMT. The remainder of this paper is structured as follows. In section II, the double-pulse test setup used in this study is proposed. In section III, the self-sustained oscillation which occurs at turn-off transient of cascode GaN HEMT is identified. In section IV, the impact of gate loop beads and power loop beads is investigated. In section V, an analytical model is proposed to analyze the instability of the half-bridge circuit utilizing power loop beads. Based on the model, a design method for the power loop beads is proposed in section VI. The design method is validated by the test data in section VII. In the end, the power loop beads optimum design procedures are presented in section VIII.

II. Double-Pulse Test Setup

To obtain the turn-off waveforms of the cascode GaN HEMTs, the double-pulse test is performed. Figure 1 shows the double-pulse test platform and the equivalent double pulse test circuit. In the test circuit, the device under test (DUT) T_1 is 650V/20A Transphorm cascode GaN HEMTs TPH3208PS. The freewheeling diode D_2 is the 650V/26A SiC Schottky diode CVFD20065A. $R_{GE} = 27\Omega$ is the external gate resistor. V_{DC} is the DC-bus voltage. $C_{DC} = 470\mu F$ is the power capacitor. An air coil inductor $L_0 = 277\mu H$ is used as a load inductor. A function generator is connected to the gate driver, which generates the gate voltage V_{gg}. In the double test, V_{gg} switches with 0V/10V. A high voltage

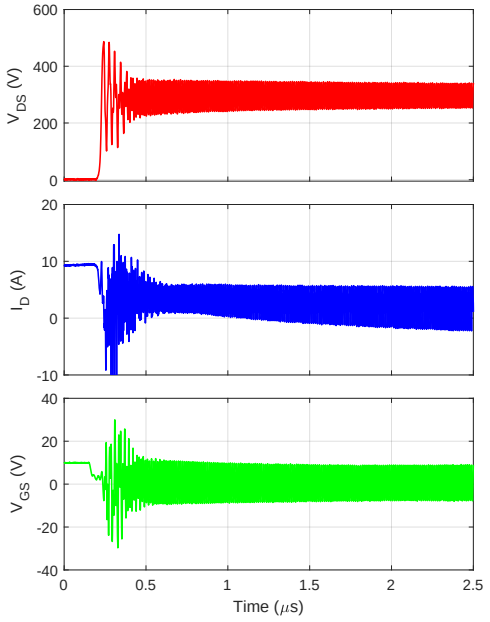

Fig. 2. Experimental turn-off waveforms with $V_{DC} = 300V$ and $I_T = 10A$.

differential probe THDP0200 is used to measure the drain-source voltage V_{DS}. A current shunt resistor SSDN-015 is used to measure the drain current I_D. In this study, the DC-bus voltage $V_{DC} = 300V$ and load current $I_L = 10A$.

In the beginning, the double-pulse test is preformed without utilizing ferrite beads to show the unstable turn-off oscillation of cascode GaN HEMTs. Then various kinds of ferrite beads will be utilized in the gate loop (at position A) and power loop (at position B) to investigate the impact of gate loop and power loop ferrite beads on the turn-off oscillation.

III. Turn-Off Oscillation of Cascode GaN HEMTs

Fig. 2 shows experimental turn-off waveforms without utilizing ferrite beads. Self-sustained oscillation is observed during the turn-off transient. According to [8], the self-sustained oscillation occurs due to the instability of the test circuit. Due to the cascode configuration, a positive feedback mechanism can be triggered. If the test circuit is unstable, the positive feedback action can draw additional energy from the power supply, which compensates for the power losses dissipated by the resistive components in the test circuit [8]. The oscillation is thereby able to maintain self-sustaining. In this case, the test circuit is unstable when $V_{DC} = 300V$, which gives rise to the occurrence of self-sustained oscillations.

IV. Influences of Ferrite Beads on the Turn-Off Oscillation

Ferrite beads can be utilized to suppress the turn-off oscillations. The damping effect of the ferrite beads originate from the following aspects:

1) The ferrite beads generate high-frequency losses. The high power dissipation thereby becomes higher than the energy drawn by the positive feedback action. The turn-off oscillation can not maintain self-sustaining and thereby attenuates.

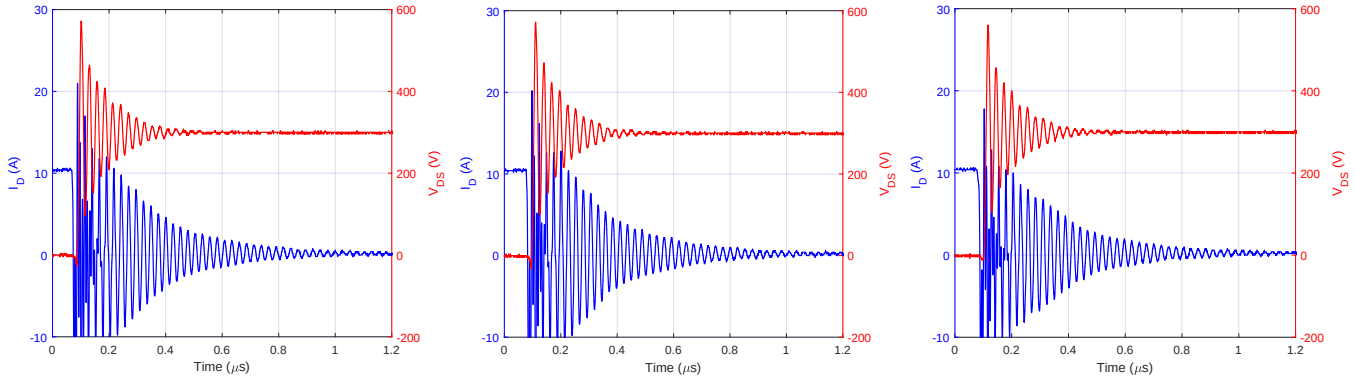

(a) $Z_F = 50\Omega$ (b) $Z_F = 120\Omega$ (c) $Z_F = 300\Omega$

Fig. 3. Experimental 300V/10A turn-off waveforms with (a) $Z_F = 50\Omega$, (b) $Z_F = 120\Omega$ and (c) $Z_F = 300\Omega$ utilized in the gate loop.

2) The ferrite beads introduce additional stray elements in the test circuit, which impact the system instability. If the circuit is more stable, the turn-off oscillation is dampened.

It should be noticed that the second aspect greatly relies on the design of the ferrite beads. If the ferrite beads introduce proper stray elements that can make the test circuit stable, the turn-off oscillation is suppressed. In the following sections, the impacts of the gate loop beads and power loop beads on the turn-off oscillation of cascode GaN HEMT are discussed.

A. *Influence of gate loop Beads*

In the previous research, it is widely proved that the gate loop beads have a very strong damping effect on the switching oscillation of non-cascode power devices like SiC MOSFETs [17] and P-GaN HEMTs [18]. Since the ferrite beads can not dissipate massive power in the gate loop, their damping effect is mainly due to the impact on the instability of the test circuit. During the oscillatory transient, the power loop can resonate with the gate loop [19], which induces self-sustained turn-off oscillation. With a ferrite bead utilized in the gate, the resonant frequency in the gate loop can be shifted far away from that in the power loop [18]. As a result, a stable test circuit is achieved, which greatly dampens the turn-off oscillation.

To investigate the impact of gate loop bead on the turn-off oscillation of cascode GaN HEMT, double-pulse tests are performed with a few different kinds of ferrite beads utilized in the gate loop. The gate bead impedance recommended by the manufacturer ranges from 30 Ω to 330 Ω at 100 MHz [10]. Within this range, the ferrite beads KMZ1608DHR500CTDH5, 74279262, and MMZ1608S301ATA00 are utilized at the position A at the gate loop, as shown in Fig. 1b. Their impedances at 100 MHz are 50 Ω, 120 Ω and 300 Ω, respectively. With the these ferrite beads utilized, the double-pulse test is performed at $V_{DC} = 300V$ and $I_L = 10A$, as shown in Fig. 3. It can be noticed that the damping effect of the gate loop beads is very weak. The underdamped oscillation can maintain for a long time before it vanishes.

The weak damping effect of gate loop bead is due to the cascode configuration of the cascode GaN HEMTs. Fig. 4 shows the cascode GaN HEMT based resonant circuit with

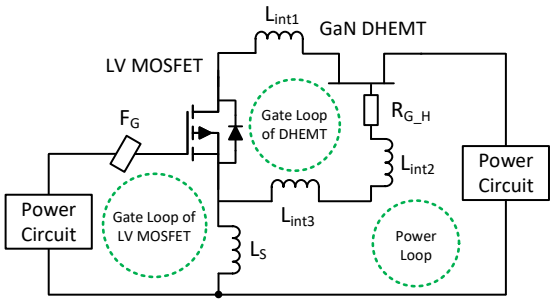

Fig. 4. Cascode GaN HEMT based resonant circuit with ferrite beads in the gate loop.

a ferrite bead F_G utilized in the gate loop. Due to the cascode configuration, the cascode GaN HEMTs have two gate loops: one is at the gate-side of LV MOSFET and the other is at the gate-side of DHEMT, as shown in Fig. 4. In the gate loop of DHEMT, the gate resistance R_{G_H} is designed to be very small to achieve high switching speed [20] and avoid unwanted reliability issues [3]. The gate loop of the DHEMT thereby does not have effective damping. With the F_G utilized, the gate loop of the DHEMT can still resonate with the power loop and excite underdamped turn-off oscillation. Therefore, the damping effect of the gate loop beads on the turn-off oscillation is relatively weak.

With a weak damping effect, the gate loop can not suppress the turn-off oscillation. Therefore, utilizing ferrite beads in the gate loop is not a good option for the circuit design.

B. *Influences of power loop Beads*

Utilizing ferrite beads in the power loop is widely proved to be very effective to suppress the turn-off oscillation of cascode GaN HEMTs [10], [13], [14]. The power loop beads can greatly suppress the oscillation due to the following reasons:

1). In the power loop, the ferrite beads can generate high-frequency losses to dampen the turn-off oscillation.

2). The power loop beads shift the power loop resonant frequency far away from that of the other two gate loops, which can disrupt the turn-off oscillation.

If optimum designed power loop beads are utilized, the oscillation is mainly suppressed due to the second reason. In this

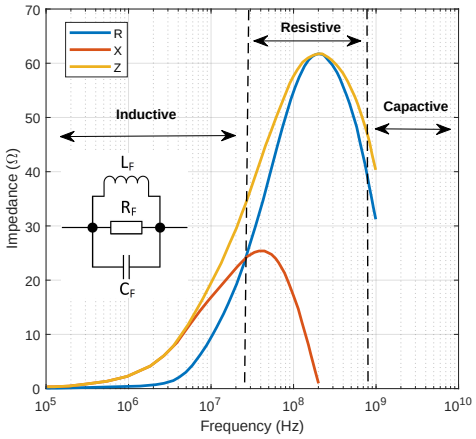

Fig. 5. Impedance-frequency plot of a typical ferrite bead indicating its equivalent circuit model.

case, the test circuit becomes very stable, which greatly dampens high-frequency oscillation. The high-frequency losses on the ferrite beads should be relativity minor. As a result, the turn-off oscillation is suppressed without an increase in the overall power losses.

However, the introduction of the power loop beads also has a major drawback. The ferrite beads also introduce additional stray inductance in the power loop, which can make the test circuit more instable. In the worst-case scenario, extra oscillation can be excited if improper ferrite beads are utilized [15], [16]. To solve this problem, an analytical approach is developed in this study to obtain an optimum design of the power loop beads, which is presented in the following sections.

V. Analytical Modeling of the Test Circuit Utilizing Power Loop Beads

To investigate the instability of the test circuit using the power loop beads, a small-signal model is derived following the approach presented in [8], [19], [21]–[24]. Fig. 5 shows the impedance-frequency plot of a typical ferrite bead. A ferrite bead can be modelled as a parallel-connected inductor L_F, resistor R_F, and capacitor C_F [25], which correspondences to the inductive, resistive, and capacitive response regions presented in Fig. 5. The dc resistance of the power ferrite beads is extremely small and is thereby neglected in this analysis.

Fig. 6a shows the schematic of the double-pulse circuit with a power ferrite bead F_P utilized in the power loop. L_P is the power loop inductance, which includes the power loop stray inductance and stray inductance of drain lead. L_G is the gate loop inductance, which includes the gate loop stray inductance and stray inductance of gate lead. L_S is the stray inductance in the common source.

To analyze the circuit instability, the test circuit presented in Fig. 6a is converted to its equivalent small-signal model [21]–[23], [26]. With the equivalent ferrite bead model utilized, the small-signal model is derived, as shown in Fig. 6b. In the model, R_F, L_F, and C_F are the stray resistance, inductance, and capacitance of the power loop bead F_P. Following the approach proposed in [23], [26], the DC-bus voltage V_{DC}

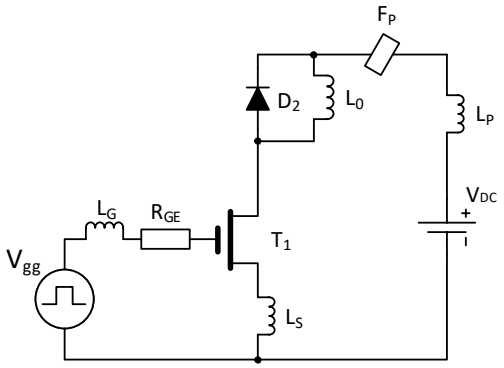

(a) Double-pulse test circuit.

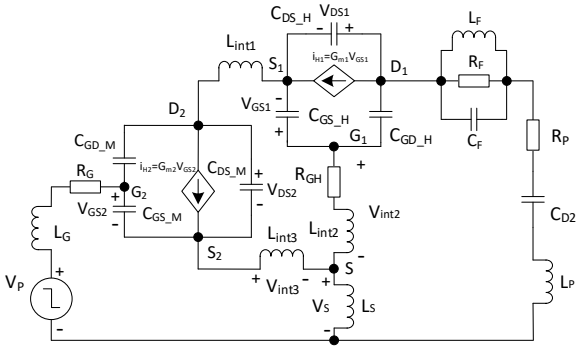

(b) Small-signal model.

Fig. 6. Double-pulse test ciruit with ferrite beads utilized in the power loop. (a) Test circuit schematic. (b) Equavilent small-signal model.

is short-circuited. The high-side freewheeling diode D_2 is replaced by its capacitance C_{D2}. The gate drive voltage V_{gg} is replaced by its small signal V_P. Following the approach presented in [27], the V_P is generally considered as a non-zero small signal since it does not have any impact on the system instability. R_G is the gate resistance, which includes the internal gate resistance R_{GI} and external gate resistance R_{GE}. R_P is the power loop stray resistance, which includes the stray resistances of the device and power loop. The GaN cascode HEMT is replaced by its equivalent small-signal model. In the model, $L_{int1(2,3)}$ are the stray inductances of the internal bond wire interconnections. R_{GH} is the internal gate resistance of the DHEMT. C_{GS_M}, C_{GD_M} and C_{DS_M} are the gate-source, gate-drain and drain-source capacitances of the LV MOSFET. C_{GS_H}, C_{GD_H} and C_{DS_H} are the gate-source, gate-drain and drain-source stray capacitances of the DHEMT. Following the approach presented in [21]–[23], [26], the small-signal of the channel current $I_{CH1(2)}$ can be modelled as $i_{H1(2)} = G_{m1(2)} \cdot v_{GS1(2)}$, where G_{m1} and G_{m2} are transconductance of the DHEMT and LV MOSFET, respectively.

By analysing the node current in G_1, D_1, S_1, S, G_2, S_2 and D_2, the equations (1)-(8) can be obtained, which are presented as follows:

$$V_P - (V_{GS2} + V_{int3} + V_S)/R_G + sL_G - sV_{GS2}C_{GS\_M} - s(V_{GS2} - V_{DS2})C_{GD\_M} = 0 \quad (1)$$

$$\frac{V_{int3}}{sL_{int3}} - sV_{GS2}C_{GS\_M} - G_{m2}V_{GS2} - sV_{DS2}C_{DS\_M} = 0 \quad (2)$$

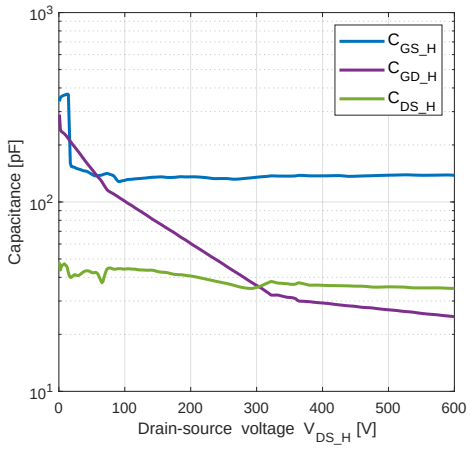

Fig. 7. C-V characteristics of the GaN DHEMT.

$$s(V_{DS2}-V_{GS2})C_{GD\_M}+sV_{DS2}C_{DS\_M}+G_{m2}V_{GS2} -(V_{int2}-V_{GS1}-V_{DS2}-V_{int3})/sL_{int1}=0 \quad (3)$$

$$V_{int2}/(sL_{int2}+R_{GH})-s(V_{DS1}-V_{GS1})C_{GD\_H} +sV_{GS1}C_{GS\_H}=0 \quad (4)$$

$$sV_{DS1}C_{DS\_H}+sV_{GS1}C_{GS\_H}+G_{m1}V_{GS1} -(V_{int2}-V_{GS1}-V_{DS2}-V_{int3})/sL_{int1}=0 \quad (5)$$

$$s(V_{DS1}-V_{GS1})C_{GD\_H}+sV_{DS1}C_{DS\_H} +G_{m1}V_{GS1}+(V_S+V_{int2}-V_{GS1}+V_{DS1})/Z_P \quad (6)$$

$$Z_P=1/((1/R_F)+(1/(SL_F))+(SC_F)) +sL_P+R_P+1/(SC_{D2}) \quad (7)$$

$$V_{int3}/sL_{int3}+V_{int2}/(sL_{int2}+R_{GH})-V_S/sL_S=0 \quad (8)$$

Where the voltage components $V_{GS1(2)}$, $V_{DS1(2)}$, $V_{int2(3)}$ and V_S are defined in Fig. 6b. The system of linear equations (1)-(8) has nine varibles: V_{GS1}, V_{GS2}, V_{DS1}, V_{DS2}, V_{int2}, V_{int3}, V_S, V_P and Z_P. With the MATLAB symbolic math toolbox utilized, the varibles V_{GS1}, V_{DS1}, V_{DS2}, V_{int2}, V_{int3}, V_S and Z_P can be eliminated. The equations (1)-(8) are thereby simplified to a equation that contains variables V_{GS2} and V_P. During the oscillatory transient, the gate drive voltage V_P provides the initial disturbance signal in the gate. Therefore, V_P is input of the oscillatory system. Using V_{GS2} as the system output, the transfer function $H(s)$ of the oscillatory system is obtained as:

$$H(s)=\frac{V_{GS2}}{V_P} \quad (9)$$

The $H(s)$ is of the ninth order. Therefore, it is impossible to solve $H(s)$ analytically. The poles of $H(s)$ are thereby derived numerically by MATLAB.

To analyze transfer function $H(s)$, its parameters should be obtained. Following the approach proposed in [19], [21]–[23], [26], [28], the nonlinear behaviour of resonant circuit is neglected. The parameters can thereby be extracted at their dc operating point. In the device under test, a silicon MOSFET IRF8707 is utilized to drive a normally-on GaN DHEMT [19]. Following the approach presented in [19], [21], the stray capacitances of the LV MOSFET are linearized at it is off-state voltage $V_{DS\_M(off)}$. According to the SPICE simulation results, $V_{DS\_M(off)} \approx 24V$. Based on the C-V curves obtained from the device datasheet [29], the capacitances C_{GD_M}, C_{GS_M} and C_{DS_M} are extracted at $V_{DS\_M(off)}$, as shown in Table I.

TABLE I
PARAMETERS OF THE DEVICE UNDER TEST

Symbol	Value	Symbol	Value	Symbol	Value
R_{GI}	2.2 Ω	R_P	0.4 Ω	R_{GH}	0.12 Ω
C_{D2}	1.09 nF	G_{m1}	0.08 S	G_{m2}	0.07 S
L_P	7.6 nH	L_S	0.8 nH	L_G	5.9 nH
L_{int1}	0.26 nH	L_{int2}	0.2 nH	L_{int3}	0.33 nH
C_{GD_M}	71.8 pF	C_{GS_M}	653.7 pF	C_{DS_M}	66.9 pF
C_{GD_H}	40.8 pF	C_{GS_H}	132.5 pF	C_{DS_H}	35.4 pF
L_F	$0.037\mu H$	C_F	0.589 pF	R_F	120 Ω

Fig. 7 shows the C-V curves of GaN DHEMT provided by the device manufacturers. Based on the C-V characteristics, the capacitances C_{GD_H}, C_{GS_H} and C_{DS_H} are extracted at $V_{DC}-V_{DS\_M(off)}$. During the turn-off transient, the freewheeling diode D_2 forward conducts, the capacitance C_{D2} is thereby linearized at 0V. The capacitances C_{D2} of D_2 are thereby extracted at 0V. Following the approach presented in [19], [21], [22], the transconductance G_{m1} and G_{m2} are extracted at the threshold voltages of DHEMT and LV MOSFET, respectively. The circuit stray inductances L_P and L_G are obtained by the Q3D extractor. The internal stray elements R_{GH}, $L_{int1(2,3)}$ and L_S are extracted from the SPICE model provided by the manufacturer. The R_{GI} is obtained from the device datasheet [29]. The R_F, L_F, and C_F are extracted from the circuit model of a TDK ferrite bead with part number MAF1608GAD121LTAH0. In the next section, the parameters of the ferrite bead will vary depending on the bead utilized in the power loop. The values of all the parameters are summarized in Table I.

To identify the impact of ferrite beads on the turn-off oscillation, its instability of transfer function $H(s)$ should be analysed. Since the instability of $H(s)$ is mainly determined by its poles, the poles of $H(s)$ should thereby be investigated. Utilizing the parameters presented in Table I, the poles of the $H(s)$ are calculated, as shown in Fig. 8. The P_1, P_3, and P_5 are real poles, whereas P_2, P_2^*, P_4, P_4^*, P_6 and P_6^* are the complex conjugate pole pairs.

In Fig. 8a, the real poles P_1, P_3, and P_5 do not have impact on the system instability. The conjugate pole pairs P_2 and P_2^* lay far away from the imaginary axis, their impact on the system instability is thereby negligible. To shows the conjugate pole pairs P_4, P_4^*, P_6 and P_6^*, Fig. 8a is zoomed, as shown in Fig. 8b. Compared with the other complex conjugate pole pairs, the P_6 and P_6^* lie much closer to the imaginary axis.

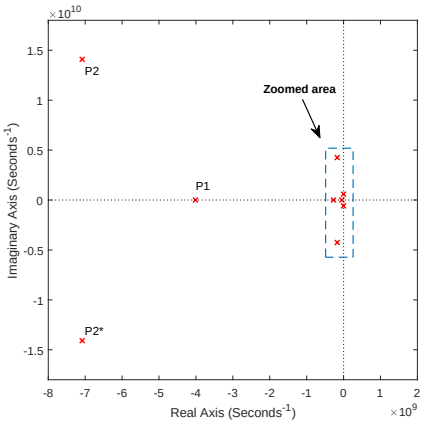

(a) Plot of poles

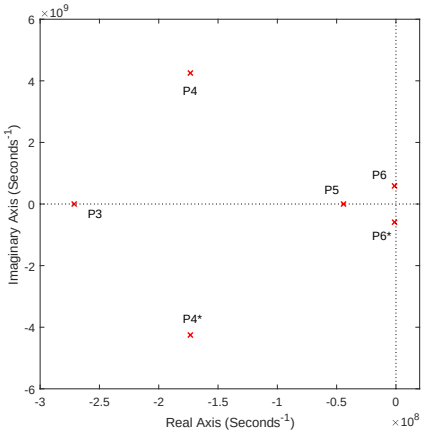

(b) Zoomed plot

Fig. 8. Poles of transfer function $H(s)$: (a) Plot of poles; (b) Zoomed plot of poles.

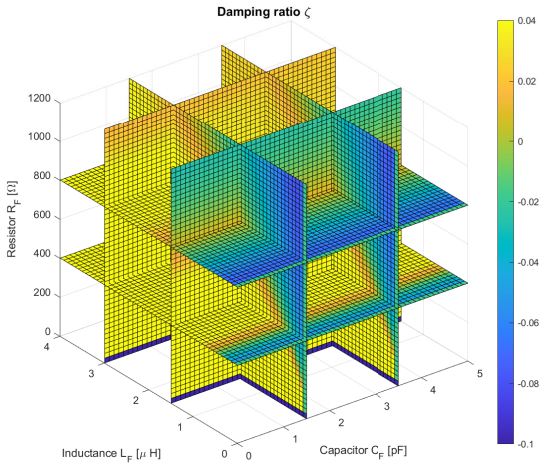

(a) Plot of poles

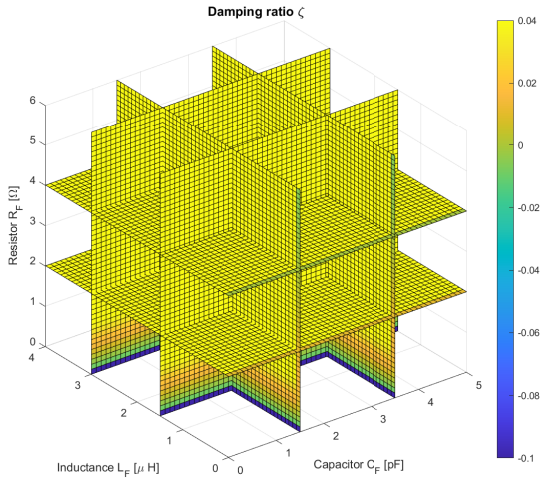

(b) Zoomed plot

Fig. 9. Plots of ζ: (a) ζ as a function of R_F, L_F and C_F; (b) Zoomed plot of Fig. 9a with $R_F \in [0\Omega, 6\Omega]$.

Therefore, the instability of the test circuit is dominated by P_6 and P_6^*.

In the next few sections, the damping ratio ζ of P_6 and P_6^* is used to analyze the system instability. ζ can be obtained by $\zeta = \sigma/(\sigma^2 + \omega^2)$, where the -$\sigma$ and ω are the real and imaginary parts of P_6 and P_6^*. When $\zeta < 0$, the oscillatory system is unstable and the self-sustained oscillation can be excited. When $\zeta > 0$, the system is stable and the oscillation attenuates.

VI. Power Loop Beads Optimum Design

To clarify the optimum design on the power loop bead F_P, the impact of R_F, L_F and C_F on the damping ratio ζ of P6 is analyzed. Fig. 9a shows the plot of ζ in volume slice planes as a function of R_F, L_F and C_F. Fig. 9b shows the zoomed plot of Fig. 9a with $R_F \in [0\Omega, 6\Omega]$. It can be noticed that ζ is independent of stray capacitance C_F and is only determined by the stray resistance R_F and inductance L_F. This is because the turn-off oscillation frequency (tens of megahertz, as shown in Fig. 2) is far below the typical frequency range of capacitive region (hundreds of megahertz to few gigahertz, as shown in Fig. 5). Therefore, the impact of stray capacitance C_F on the turn-off oscillation can be neglected. In 9b, it is also shown that R_F mainly determine ζ when R_F have very small resistance.

Since ζ is independent of C_F, the impact of R_F and L_F on ζ should be investigated. Fig. 10a shows the plot of ζ as a function of R_F with various L_F. When R_F is small, the damping effect of R_F is significant. The ζ becomes larger with the increase of R_F. However, when R_F is large enough, the ferrite bead becomes more inductive with the increase of R_F, which results in the reduction of ζ, as shown in Fig. 10a. With the increase of L_F, the peak value of ζ increases and eventually plateaus at maximum damping ratio ζ_{max} when $L_F \geq 2nH$. In the plateau, maximum effective damping on the turn-off oscillation is achieved. The plateau is thereby the stable region for the oscillatory system. As shown in Fig. 10a, the lower boundary of the stable region is fixed at about 1 Ω. The upper boundary is indicated as R_{F_U}, which increases when L_F becomes larger. The stable region extends with the increases of L_F. To achieve effective damping, the R_F of the power ferrite bead is at least tens of ohms, which is much larger than the lower boundary. Therefore, only $R_F \leq R_{F\_U}$ is needed to be considered in the ferrite bead design.

Fig. 10b shows the plot of ζ as function of L_F. When $R_F \leq 1\Omega$, ζ increases when L_F becomes larger and plateaus at its

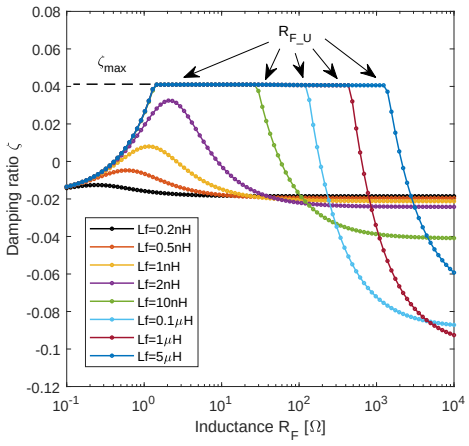

(a)

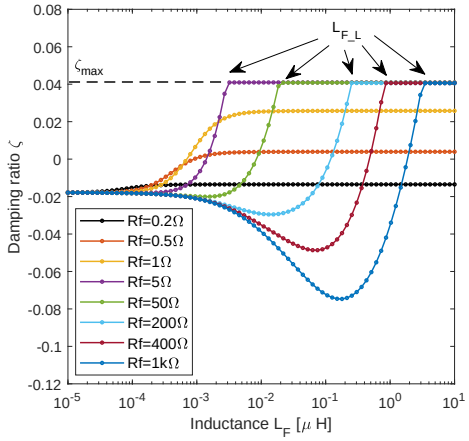

(b)

Fig. 10. Plot of ζ : (a) ζ as a function of R_F with various L_F; (b) ζ as a function of L_F with various R_F.

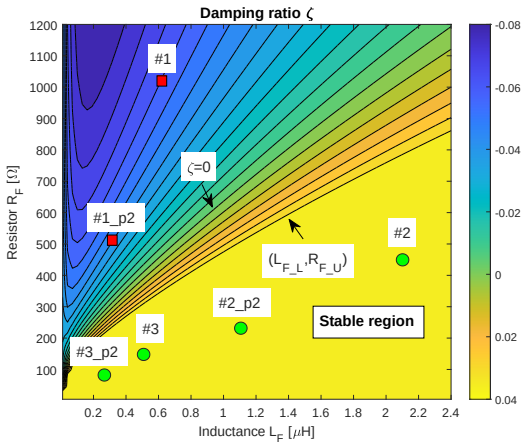

(a)

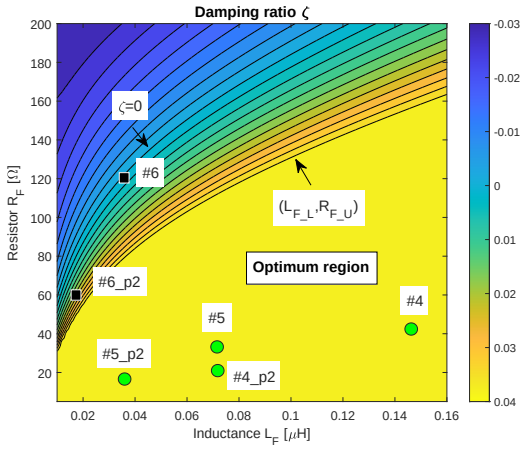

(b)

Fig. 11. Contour plot of ζ with the various desgin points (green dots indicate $\zeta = \zeta_{max}$, black squares indicate $\zeta \in (0, \zeta_{max})$ and red squares indicate $\zeta < 0$) : (a) ζ as a function of L_F and R_F with $L_F \in [10nH, 2.4\mu H]$ and $R_F \in [5\Omega, 1.2k\Omega]$; (b) Zoomed plot of Fig. 11a with $L_F \in [10nH, 160nH]$ and $R_F \in [5\Omega, 200\Omega]$.

maximum value. The maximum value is smaller than ζ_{max} since the small R_F limit the effective damping of the bead. When $R_F \geq 5\Omega$, ζ reduces with the increase of L_F in the beginning, as shown in Fig. 10b. In this phase, the power loop resonant frequency is close to that of the gate loops. With larger L_F, the power loop bead becomes more inductive. This makes the oscillatory system more unstable, which give rise to the initial reduction of ζ. However, when L_F is large enough, the ζ starts to raise with the increase of L_F, as shown in Fig. 10b. In this phase, the power loop resonant frequency becomes much smaller than that of the gate loops and system resonance is disrupted. With the increase of L_F, the power loop resonant frequency becomes lower, which gives rise to a more stable oscillatory system. As a result, ζ raises with the increase of L_F. In the end, ζ plateaus at $\zeta = \zeta_{max}$ and the stable region is achieved. In Fig. 10b, the lower boundary of the stable region is indicated as L_{F_L}. With the increase of R_F, L_{F_L} becomes larger, which gives rise to a narrower stable region. To ensure that the oscillatory system operates in the stable region, the $L_F \geq L_{F\_L}$ is required.

The contour plot of ζ as a function of L_F and R_F with $L_F \in [10nH, 2.4\mu H]$ and $R_F \in [5\Omega, 1.2k\Omega]$ is presented in Fig. 11a. The contour line with $\zeta = 0$ is indicated. In the contour plot, the stable region is yellow area under the contour line (L_{F_L}, R_{F_U}), as shown in n Fig. 11a. In the stable region, with $L_F \geq L_{F\_L}$ and $R_F \leq R_{F\_U}$, maximum damping ratio ζ_{max} is achieved. The maximum effective damping on the turn-off oscillation is thereby achieved when the L_F and R_F of the power loop beads lay in the stable region.

It should be noticed that a large stray inductance L_F can also introduce additional stray inductance in the power loop. This causes the high voltage overshoot during the turn-off transient. To minimize the voltage overshoot, the L_F should be very small. Fig. 11b shows the zoom contour plot of Fig. 11a with $L_F \in [10nH, 160nH]$ and $R_F \in [5\Omega, 200\Omega]$. The yellow area under the contour line (L_{F_L}, R_{F_U}) is a optimum region which can achieve both the small L_F and $\zeta = \zeta_{max}$. If the design points $(L_{F(n)}, R_{F(n)})$ of the power loop beads locates in the optimum region, power loop beads should suppress the turn-off oscillation while mitigating the voltage overshoot. As a result, an optimized turn-off performance is achieved for the cascode GaN HEMTs.

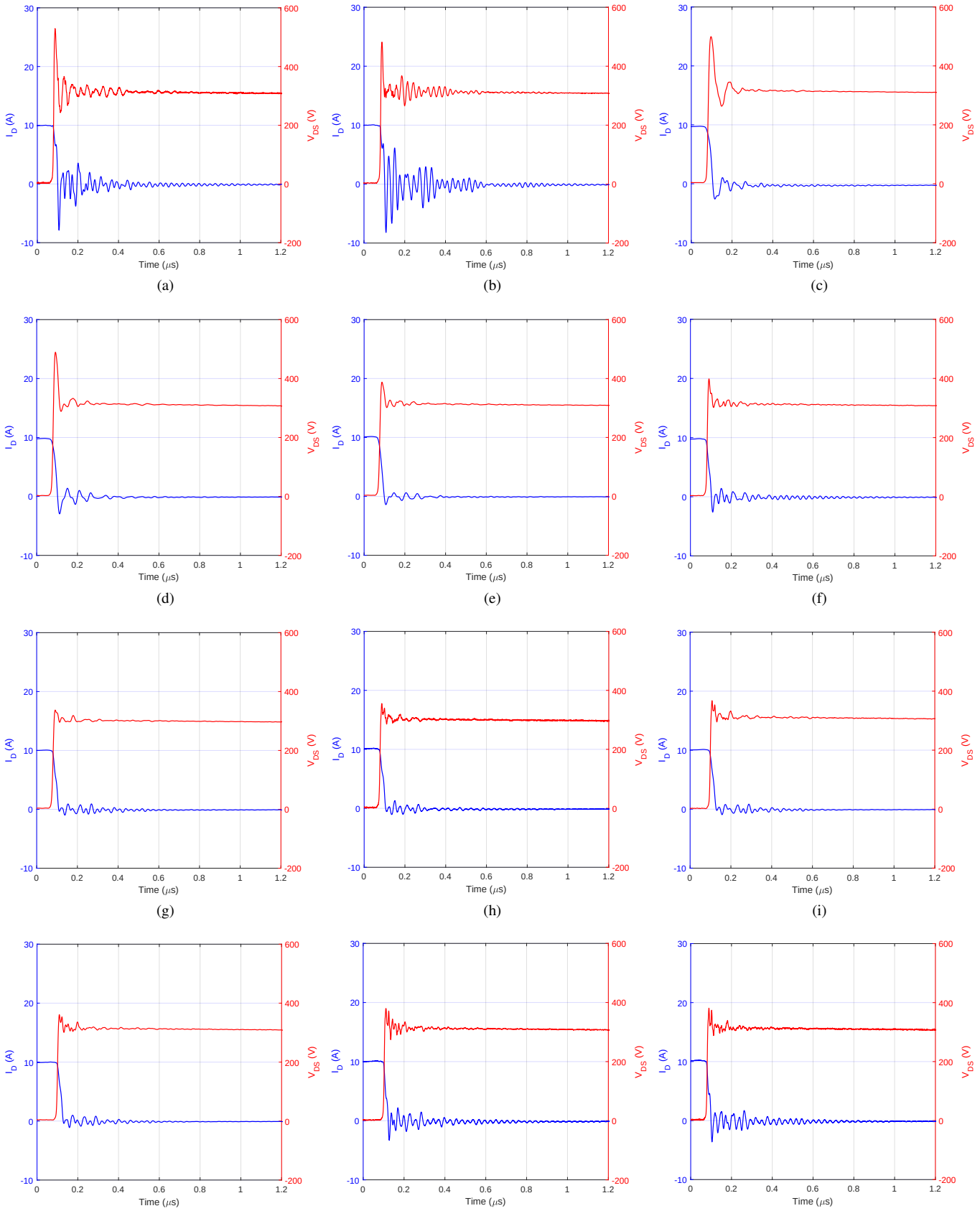

Fig. 12. Experimental 300V/10A turn-off waveforms using following power loop beads: (a) single #, (b) two paralleled #1 , (c) single #2 , (d) two paralleled #2, (e) single #3, (f) two paralleled #3, (g) single #4, (h) two paralleled #4, (i) single #5, (j) two paralleled #5, (k) single #6 and (l) two paralleled #6.

TABLE II
FERRITE BEADS UTILIZED IN THE POWER LOOP.

Bead	Part number	Z_F	R_F	L_F
#1	74279252	880 Ω	1012 Ω	0.633 μH
#2	7427511	416 Ω	450 Ω	2.1 μH
#3	742792511	190 Ω	152 Ω	0.482 μH
#4	BLM21SN300SZ1D	30 Ω	40.8 Ω	0.146 μH
#5	MPZ1608S260ATDH5	26 Ω	34 Ω	0.072 μH
#6	MAF1608GAD121LTAH0	20 Ω	120 Ω	0.037 μH

VII. EXPERIMENTAL VALIDATION

To validate the optimum design method proposed in the previous section, the double-pulse test is performed with ferrite beads utilized in the position B in the power loop, as shown in Fig. 1b. Six different kinds of ferrite beads are utilized, which are denoted as beads #n (n=1-6), as shown in Table II. Their impedance Z_F (at 100 MHz), stray resistance R_F and inductance L_F are also provided in the table. The Z_F is obtained from the datasheet. The R_F and L_F are extracted in the equivalent model provided by the manufacturer. To validate the proposed design method, the power loop beads are required to achieve 'good' and 'bad' design points. This greatly limited the choice of the power loop beads. Some ferrite beads which have dc current ratings lower than 10A is thereby selected to achieve specific design points. Fortunately, the ferrite beads do not generate much heat in double-pulse test and can work under much higher load current than their maximum dc current ratings. Therefore, there is no need to consider current limitation of ferrite beads in the double-pulse test. However, in the real application, the ferrite beads current ratings should be considered, which is discussed in the next section.

In the test, various ferrite bead designs are utilized in the power loop. At first, the test is performed with a single #n bead (n=1-6) utilized in the power loop. The corresponding design points $(L_{F(n)}, R_{F(n)})$ of the ferrite beads are indicated as #n (n=1-6) in the Fig. 11. $R_{F(n)}$ and $L_{F(n)}$ are the stray resistance and inductance of #n bead (n=1-6). The test is also performed with two #n beads (n=1-6) connected in parallel in the power loop. In this case, the equivalent stray resistance and inductance of the parallel-connected #n beads (n=1-6) become half of the single #n bead (n=1-6). Their design points $(L_{F(n)}/2, R_{F(n)}/2)$ are indicated as #n_P2 (n=1-6) in the Fig. 11. The design points are marked by green dots, black squares and red squares, which indicate the design points have $\zeta = \zeta_{max}$, $\zeta \in (0, \zeta_{max})$, and $\zeta < 0$, respectively. The experimental 300V/10A turn-off waveforms utilizing single and parallel-connected #n beads (n=1-6) are presented in Fig. 12.

As shown in Fig. 11a, the design points #2, #2_P2, #3 and #3_P2 are marked by green dots. These design points lay in the stable region and the maximum damping ratio ζ_{max} is achieved. Figs. 12 (c)-(f) show the experimental turn-off waveforms utilizing the corresponding ferrite beads. With $\zeta = \zeta_{max}$, the turn-off oscillation quickly attenuates. However, due to the large L_F, a huge voltage overshoot is observed in the test waveforms. With the increase of L_F, the peak overshoot voltage becomes higher. The design points #1, #1_P2 are marked in red squares, as shown in Fig. 11a. The experimental turn-off waveforms using the corresponding ferrite beads are given in Figs. 12 (a) and (b). With negative ζ, the resonant circuit utilizing the designs #1, #1_P2 is unstable and self-sustained oscillation can be excited. However, during the oscillatory transient, ac resistance is generated in the power loop due to the skin effect on the power loop circuit and radiation loss [30]. Due to the effective damping generated by the ac resistance, the oscillation can not maintain self-sustaining and becomes underdamped, as shown in Figs. 12 (a) and (b). The analytical results agree with the test data. It should be noticed that #1 bead has 880 Ω of impedance and still can not suppress the turn-off oscillation. This shows that ferrite beads with large impedance do not necessarily have a strong damping effect on the turn-off oscillation.

As shown in Fig. 11b, the design points #4, #4_P2, #5 and #5_P2 are marked by green dots. These design points lay in the optimum region which achieves both small L_F and maximum damping ratio ζ_{max}. The experimental turn-off waveforms utilizing the corresponding ferrite beads are shown in Figs. 12 (g)-(j). With these ferrite beads used in the power loop, the turn-off oscillation is greatly suppressed. Moreover, due to the small L_F and high ζ, the voltage overshoot is also greatly mitigated. The design points #6, #6_P2, which are marked in black squares, are given in Fig. 11b. These design points have the damping ratio $\zeta \in (0, \zeta_{max})$. The low damping ratio gives rise to the relatively weak effective damping of the ferrite beads. As a result, underdamped turn-off oscillation is excited, as shown in Figs. 12 (k) and (l). Moreover, with a small damping ratio, a relatively high overshoot voltage is observed even when L_F is very small. The test results validate that the ferrite bead designs in the optimum region can achieve the best turn-off performance for the cascode GaN HEMT.

In Fig. 12k, the oscillation frequency of the turn-off test using a single #6 beads is around 40 MHz. In Fig. 8b, the dominant pole pair P_6 and P_6^* of the corresponding oscillatory system is derived. The oscillation frequency f of the pole pair can be calculated by:

$$f = \frac{\omega}{2\pi} = 92 \text{ MHz} \tag{10}$$

The analytical and experimental results are in the same order. However, the oscillation frequency of the experimental waveform does not completely agree with that derived from the dominant pole pair P_6 and P_6^*. This is due to two reasons. Firstly, with ferrite beads and cascode GaN HEMTs used, the transfer function of the oscillatory system is very complex and has multiple complex conjugate pole pairs. The other complex conjugate pole pairs can also have a minor impact on the oscillatory system. Secondly, The proposed small-signal model greatly simplifies the oscillatory system. The ferrite beads are simplified as a parallel-connected inductor L_F, resistor R_F, and capacitor C_F. The parameters of power devices are also approximately linearized at their DC operating points. The

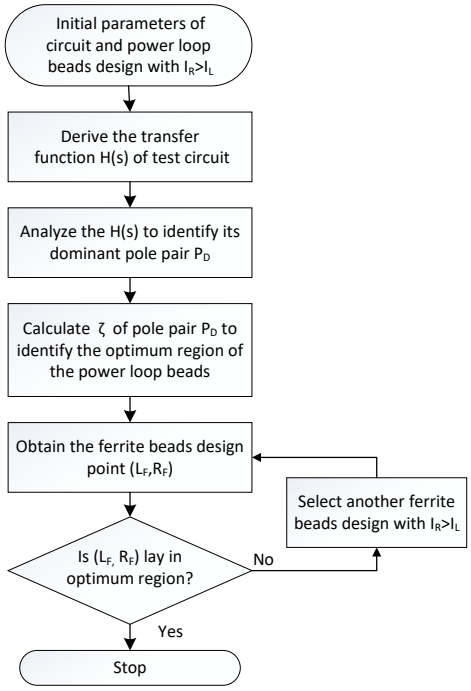

Fig. 13. Flowchart of power loop beads optimum design procudure.

non-linear behaviours of the resonant circuit, like the voltage-dependent stay capacitances, are not included. All in all, to make the analytical modelling feasible, some simplifications are needed, which cause the errors. However, the experimental results presented in Fig. 12 validate the proposed methods can provide a reasonable general guideline for the ferrite beads design.

VIII. The power loop beads design procedure

In the real application, th rated dc current I_R of the selected ferrite beads should be higher than I_L. Fig. 13 shows a flowchart of power loop beads optimum design procedure considering the current limitation of power loop beads. In the beginning, the initial ferrite beads design which achieves $I_R > I_L$ should be selected. The initial parameters of the circuit and power loop beads are thereby obtained to calculate the transfer function H(s) based on the system of linear equations (1)-(8). It should be noticed that the dominant pole pair P_D of H(s) depend on the circuit and power loop beads parameters and may not be the pole pair P6. Therefore, the analysis presented in Fig. 8 should be used to determine the dominant pole pair of H(s). After that, the damping ratio ζ can be calculated with various R_F and L_F to identify the optimum region presented in Fig. 11b. The design point (L_F, R_F) of the selected ferrite beads design are obtained to check whether the design point lay in the optimum region. If (L_F, R_F) lay in the optimum region, the optimum design of the ferrite beads is achieved. If not, another ferrite bead design with $I_R > I_L$ should be selected to identity its (L_F, R_F). The optimum design procedure stops when a ferrite beads design point lays in the optimum region.

IX. Conclusion

This paper presents a detailed analysis of the optimum design on the ferrite beads in the cascode GaN HEMT-based half-bridge test circuit. Based on the theoretical analysis and experimental investigation, it is identified that the ferrite beads have a weak damping effect when they are utilized in the gate loop. To obtain the optimum design of power loop beads, an analytical model is derived to obtain the transfer function of the test circuit. The analysis on a dominant pole of transfer function reveals the stray capacitance C_F of the power loop bead does not have a significant impact on system instability. The oscillatory system can achieve maximum damping ratio ζ_{max} when the stray inductance L_F, the resistance R_F of the power loop bead are in a certain range. A stable region is identified to design the power loop bead which can suppress the oscillation. Since the power loop bead can introduce high stray inductance in the power loop, a high voltage overshoot can be excited even when the turn-off oscillation is suppressed. An optimum region is thereby identified to design a power loop bead that can suppress the oscillation while mitigating the voltage overshoot. The accuracy of the proposed design method is validated by the test results. The proposed ferrite beads design method can also be used in the other cascode device like SiC JFET Cascode.

References

[1] X. Huang, Z. Liu, Q. Li, and F. C. Lee, "Evaluation and application of 600 v GaN HEMT in cascode structure," *IEEE Transactions on Power Electronics*, vol. 29, no. 5, pp. 2453–2461, 2014, DOI: 10.1109/TPEL.2013.2276127.

[2] X. Huang, Q. Li, Z. Liu, and F. C. Lee, "Analytical loss model of high voltage GaN HEMT in cascode configuration," *IEEE Transactions on Power Electronics*, vol. 29, no. 5, pp. 2208–2219, 2014, DOI: 10.1109/TPEL.2013.2267804.

[3] R. Siemieniec, G. Nöbauer, and D. Domes, "Stability and performance analysis of a sic-based cascode switch and an alternative solution," *Microelectronics Reliability*, vol. 52, no. 3, pp. 509–518, 2012, DOI: 10.1016/j.microrel.2011.12.006.

[4] X. Huang, W. Du, F. C. Lee, Q. Li, and W. Zhang, "Avoiding divergent oscillation of a cascode GaN device under high-current turn-off condition," *IEEE Transactions on Power Electronics*, vol. 32, no. 1, pp. 593–601, 2017, DOI: 10.1109/TPEL.2016.2532799.

[5] Z. Xu, W. Zhang, F. Xu, F. Wang, L. M. Tolbert, and B. J. Blalock, "Investigation of 600 V GaN HEMTs for high efficiency and high temperature applications," in *Applied Power Electronics Conference and Exposition*, 2014, pp. 131–136, DOI: 10.1109/JESTPE.2016.2563220.

[6] L. He, Z. Xuan, L. Wen, J. A. Brothers, and W. Jin, "Paralleled operation of high voltage Cascode GaN HEMTs," *IEEE Journal of Emerging & Selected Topics in Power Electronics*, vol. 4, no. 3, pp. 815–823, 2017, DOI: 10.1109/JESTPE.2016.2557316.

[7] W. Zhang, X. Huang, F. C. Lee, and Q. Li, "Gate drive design considerations for high voltage cascode GaN HEMT," in *IEEE Applied Power Electronics Conference and Exposition*, 2014, pp. 1484–1489, DOI: 10.1109/APEC.2014.6803503.

[8] P. Xue and F. Iannuzzo, "Self-sustained Turn-off Oscillation of Cascode GaN HEMTs: Occurrence Mechanism, Instability Analysis and Oscillation Suppression," *IEEE Transactions on Power Electronics*, vol. 37, no. 5, pp. 5491–5500, 2022, Early Access, DOI: 10.1109/TPEL.2021.3131535.

[9] M. Pajnić, P. Pejović, Ž. Despotović, M. Lazić, and M. Skender, "Characterization and gate drive design of high voltage cascode GaN HEMT," in *2017 International Symposium on Power Electronics*, 2017, pp. 1–5, DOI: 10.1109/PEE.2017.8171670.

[10] H. Zan and C. Jason, "Recommended external circuitry for transphorm GaN FETs," Application Note AN0009, 2016.

[11] Z. Huang and J. Cuadra, "Preventing GaN Device VHF Oscillation," presented at APEC 2017 Industry Session, March 2017.

[12] Z. Wang, J. Honea, and Y. Wu, "Design and implementation of a high-efficiency three-level inverter using GaN HEMTs," in *Proceedings of PCIM Europe 2015*, 2015, pp. 1–7.

[13] T. Zhu, F. Zhuo, F. Zhao, F. Wang, and T. Zhao, "Quantitative model-based false turn-on evaluation and suppression for cascode GaN devices in half-bridge applications," *IEEE Transactions on Power Electronics*, vol. 34, no. 10, pp. 10 166–10 179, 2019, DOI: 10.1109/TPEL.2018.2890680.

[14] F. Zhao, Y. Li, Z. Chen, S. Yang, and J. Chen, "Negative Conductance Modeling and Stability Analysis of High-Frequency Oscillation Based on Cascode GaN Circuits," *IEEE Access*, vol. 8, pp. 114 100–114 111, 2020, DOI: 10.1109/ACCESS.2020.2995726.

[15] H. Li and S. Munk-Nielsen, "Challenges in switching SiC MOSFET without ringing," in *PCIM Europe 2014*, 2014, pp. 1–6.

[16] H. Huang, X. Yang, Y. Wen, and Z. Long, "A switching ringing suppression scheme of SiC MOSFET by active gate drive," in *IPEMC-ECCE Asia*, 2016, pp. 285–291, DOI: 10.1109/IPEMC.2016.7512300.

[17] S. Yin, K. J. Tseng, R. Simanjorang, and P. Tu, "Experimental comparison of high-speed gate driver design for 1.2-kV/120-A Si IGBT and SiC MOSFET modules," *IET Power Electronics*, vol. 10, no. 9, pp. 979–986, 2017, DOI: 10.1049/iet-pel.2016.0668.

[18] J. A. Bjorn, B. Szymon, U. Christian, N. H. Petersen, J. Soren, and M. N. Stig, "A fast-switching integrated full-bridge power module based on GaN eHEMT devices," *IEEE Transactions on Power Electronics*, vol. 34, no. 3, pp. 2494–2504, 2018, DOI: 10.1109/TPEL.2018.2845538.

[19] P. Xue, L. Maresca, M. Riccio, G. Breglio, and A. Irace, "Self-Sustained Turn-Off Oscillation of SiC MOSFETs: Origin, Instability Analysis, and Prevention," *Energies*, vol. 12, no. 11, p. 2211, 2019, DOI: 10.3390/en12112211.

[20] P. J. Garsed and R. A. McMahon, "Understanding the cascode switching process," in *The 1st IEEE Workshop on Wide Bandgap Power Devices and Applications*, 2013, pp. 186–189, DOI: 10.1109/WiPDA.2013.6695593.

[21] A. Lemmon, M. Mazzola, J. Gafford, and C. Parker, "Instability in half-bridge circuits switched with wide band-gap transistors," *IEEE Transactions on Power Electronics*, vol. 29, no. 5, pp. 2380–2392, 2014, DOI: 10.1109/TPEL.2013.2273275.

[22] A. Lemmon, M. Mazzola, J. Gafford, and C. Parker, "Stability considerations for silicon carbide field-effect transistors," *IEEE transactions on Power Electronics*, vol. 28, no. 10, pp. 4453–4459, 2012, DOI: 10.1109/TPEL.2012.2226473.

[23] K. Wang, X. Yang, L. Wang, and P. Jain, "Instability analysis and oscillation suppression of enhancement-mode gan devices in half-bridge circuits," *IEEE Transactions on Power Electronics*, vol. 33, no. 2, pp. 1585–1596, 2018, DOI: 10.1109/TPEL.2017.2684094.

[24] P. Xue, L. Maresca, M. Riccio, G. Breglio, and A. Irace, "Analysis on the Self-Sustained Oscillation of SiC MOSFET Body Diode," *IEEE Transactions on Electron Devices*, vol. 66, no. 10, pp. 4287–4295, 2019, DOI: 10.1109/TED.2019.2937059.

[25] E. Jefferson and L. Aldrick, "Ferrite bead demystified," *Analog Dialogue*, vol. 50, no. 2, pp. 1–6, 2016.

[26] K. Umetani, R. Matsumoto, and E. Hiraki, "Prevention of oscillatory false triggering of GaN-FETs by balancing Gate-Drain capacitance and common-source inductance," *IEEE Transactions on Industry Applications*, vol. 55, no. 1, pp. 610–619, 2019, DOI: 10.1109/TIA.2018.2868272.

[27] S. Milady, D. Silber, F. Pfirsch, and F. J. Niedernostheide, "Simulation studies and modeling of Short Circuit current oscillations in IGBTs," in *International Symposium on Power Semiconductor Devices & Ics*, 2009, DOI: 10.1109/ISPSD.2009.5157995.

[28] K. Saito, T. Miyoshi, D. Kawase, S. Hayakawa, T. Masuda, and Y. Sasajima, "Simplified Model Analysis of Self-Excited Oscillation and Its Suppression in a High-Voltage Common Package for Si-IGBT and SiC-MOS," *IEEE Transactions on Electron Devices*, vol. 65, no. 3, pp. 1063–1071, 2018, DOI: 10.1109/TED.2018.2796314.

[29] International Rectifier, "IRF8707 Power MOSFET Datasheet," [Online]. Available: http:/www.irf.com, 2007.

[30] K. Wang, X. Yang, H. Li, H. Ma, X. Zeng, and W. Chen, "An analytical switching process model of low-voltage egan hemts for loss calculation," *IEEE Transactions on Power Electronics*, vol. 31, no. 1, pp. 635–647, 2016, DOI: 10.1109/TPEL.2015.240997.

Peng Xue received the M.S., and Ph.D. degrees from Beihang University, Beijing, China in 2013 and 2017, respectively.
From 2017 to 2019, he works as a Post-Doctoral Research Fellow at University of Naples Federico II, Italy. He is currently a Post-Doctoral researcher at the Aalborg University, Denmark. His research interests include modeling, simulation, and experimental characterization of power semiconductor devices.

Francesco Iannuzzo (IEEE Senior member) received the M.Sc. degree in Electronic Engineering and the Ph.D. degree in Electronic and Information Engineering from the University of Naples, Italy, in 1997 and 2002, respectively.
He is currently a professor of reliable power electronics at the Aalborg University, Denmark, where he is also part of CORPE, the Center of Reliable Power Electronics. His research interests are in the field of reliability of power devices, condition monitoring, failure modelling and testing up to megawatts under extreme conditions. He is author or co-author of +250 publications on journals and international conferences, three book chapters and four patents, and has edited a book on Modern Power Electronic Devices (2020, IET). Besides the publication activity, over the past years he has been contributing +20 technical seminars about reliability at top-tier conferences as ISPSD, IRPS, EPE, ECCE, PCIM and APEC.
Prof. Iannuzzo currently serves as the vice-chair of the IEEE IAS Power Electronic Devices and Components Committee. In 2018 he was the general chair of the 29th ESREF, the first European conference on the reliability of electronics, and has recently been appointed general chair for the 2023 EPE-ECCE Europe conference in Aalborg.